

# Molecular Models of Hydroxide, Oxyhydroxide, and Clay Phases and the Development of a General Force Field

Randall T. Cygan,<sup>\*,†</sup> Jian-Jie Liang,<sup>†,‡</sup> and Andrey G. Kalinichev<sup>§</sup>

*Geochemistry Department, Sandia National Laboratories, Albuquerque, New Mexico 87185-0750, and Department of Geology, University of Illinois at Urbana-Champaign, Urbana, Illinois 61801*

*Received: August 6, 2003; In Final Form: November 20, 2003*

The fate of chemical and radioactive wastes in the environment is related to the ability of natural phases to attenuate and immobilize contaminants through chemical sorption and precipitation processes. Our understanding of these complex processes at the atomic level is provided by a few experimental and analytical methods such as X-ray absorption and NMR spectroscopies. However, due to complexities in the structure and composition of clay and other hydrated minerals, and the inherent uncertainties of the experimental methods, it is important to apply theoretical molecular models for a fundamental atomic-level understanding, interpretation, and prediction of these phenomena. In this effort, we have developed a general force field, CLAYFF, suitable for the simulation of hydrated and multicomponent mineral systems and their interfaces with aqueous solutions. Interatomic potentials were derived from parametrizations incorporating structural and spectroscopic data for a variety of simple hydrated compounds. A flexible SPC-based water model is used to describe the water and hydroxyl behavior. Metal–oxygen interactions are described by a Lennard-Jones function and a Coulombic term with partial charges derived by Mulliken and ESP analysis of DFT results. Bulk structures, relaxed surface structures, and intercalation processes are evaluated and compared to experimental and spectroscopic findings for validation. Our approach differs from most others in that we treat most interatomic interactions as nonbonded. This allows us to effectively use the force field for a wide variety of phases and to properly account for energy and momentum transfer between the fluid phase and the solid, while keeping the number of parameters small enough to allow modeling of relatively large and highly disordered systems. Simulations of clay, hydroxide, and oxyhydroxide phases and their interfaces with aqueous solutions combine energy minimization and molecular dynamics methods to describe the structure and behavior of water, hydroxyl, surface species, and intercalates in these systems. The results obtained to date demonstrate that CLAYFF shows good promise to evolve into a widely adaptable and broadly effective force field for molecular simulations of fluid interfaces with clays and other clay-related phases, as well as other inorganic materials characterized by complex, disordered, and often ill-determined structure and composition.

## Introduction

Molecular modeling methods have been increasingly used in the past decade to simulate a wide range of materials and to evaluate their microscopic structure, physical, and thermodynamic properties. This is especially true of clays and related hydroxide minerals where experimental structural characterization is limited by the ultrafine grain size typical of these phases. Clays and related phases present a particularly daunting set of challenges for the experimentalist and computational chemist. However, an integrated experimental and theoretical treatment can provide significant insight into understanding the structures and properties of these complex phases on a molecular level.

Clays and related layered minerals are fine grained and poorly crystalline materials. Large single crystals of clay minerals suitable for X-ray refinement studies are lacking and therefore only a few detailed structural characterizations exist.<sup>1,2</sup> Additionally, as a rule, clay minerals lack long-range order, especially with regard to the stacking behavior of clay layers.

Clay minerals also possess low crystal symmetry and have a unique chemistry that is characterized by a variety of multicomponent substitutions in the tetrahedral and octahedral sheets. These substitutions lead to a net negative charge on the clay structural layers that allows for the intercalation of solvated metal cations, and other charged complexes, within the interlayer region. Depending upon the type of structural substitution and net charge, the clay may become expandable and provide a suitable host for a variety of intercalates. Therefore clay minerals are often invoked as suitable hosts for hazardous chemical and radioactive waste materials.

Molecular computer simulations have become extremely helpful in providing an atomistic perspective on the structure and behavior of clay minerals. These studies have typically used classical Monte Carlo (MC) or molecular dynamics (MD) methods to evaluate the interlayer structure and swelling behavior of smectite clays.<sup>3–16</sup> Successful application of any computational molecular modeling technique requires the use of interatomic potentials (force fields) that effectively and accurately account for the interactions of all atoms in the modeled system.<sup>17</sup> In addition, it is highly desirable that the interaction parameters of a force field derived from, for example, quantum chemical calculation and a limited number of model

\* Corresponding author. E-mail: rtcyan@sandia.gov.

† Sandia National Laboratories.

‡ Present address: Accelrys Inc., 9685 Scranton Rd., San Diego, CA 92121-3752.

§ University of Illinois at Urbana-Champaign.

compounds be transferable. That is, the force field must be suitable for effective modeling of a wider range of other compounds.

Unfortunately, for almost all of the previous clay simulation studies, the empirical force fields used to describe the interatomic interactions required a constrained clay lattice, although some allow the degrees of freedom associated with swelling and lateral displacement of the lattice as a whole. The use of a rigid lattice can save substantial amounts of computer time, because the degrees of freedom associated with the motion of the atoms in the solid are excluded from the calculations. Such simplified models obey all fundamental mechanical conservation laws, and due to the immobility of the lattice atoms, the exchange of energy and momentum among the interacting atoms of the clay substrate and the molecules of the interlayer or interfacial fluid (inelastic interactions) is not possible. Thus, this approach introduces an a priori distortion into the atomistic description of the structural and dynamic behavior of surface and interlayer species. The magnitude of this distortion and whether it can be safely neglected ultimately depends on the characteristic time scales of the different types of relevant atomic motion and the degree of mechanical coupling between them in the simulated systems. For hydrated phases, the time scales of vibrational and librational motions for surface OH groups are comparable to those of similar motions of interlayer H<sub>2</sub>O molecules and hydrated ions in the aqueous phase. Therefore, accurate representation of the dynamics of such processes as adsorption, surface hydration and complexation, and hydrogen bonding can be inherently limited if the atoms of the substrate layer are all considered completely immobile. Surface diffusion rates of ions and water molecules can also be overestimated, and the structure of the aqueous layers at the interface can be distorted. Additionally, atomic charges in the rigid clay lattice are typically assigned values equivalent to their full formal charge, thus generating unreasonably large electrostatic potentials. More rigorous quantum mechanics methods have been applied to several clay minerals<sup>18–21</sup> but these have been limited to fairly simple clay structures. Full structural optimizations for the large unit cells characteristic of clay phases remain too cost-prohibitive using these electronic structure methods.

Recently, Teppen et al.<sup>22</sup> were successful in developing a new force field for clay phases that was based on a rigorous analysis of experimental X-ray diffraction data and charge assignment from quantum mechanics calculations. The developed set of bonded interaction terms was successfully used to simulate several simple clay structures including gibbsite, kaolinite, pyrophyllite, and the smectite beidellite. However, in this approach bonds must be identified and evaluated for each metal–oxygen coordination. Most unique in this study is the use of an O–Al–O angle bend potential to simultaneously treat both tetrahedrally and octahedrally coordinated aluminums. In addition to tetrahedral substitution for silicon, aluminum often occurs in the octahedral sheet in clay minerals, and prior to the Teppen et al. study<sup>22</sup> there was no published force field that could be used to properly evaluate the effect of this octahedral coordination.

Zeolite-based force fields<sup>23–26</sup> that are typically incorporated in a variety of catalysis and industrial molecular modeling applications include only tetrahedral aluminum. More recently, Bougeard et al.,<sup>21</sup> as an extension of their earlier study that used fixed atomic positions for the clay,<sup>27</sup> completed molecular dynamics and vibrational spectra calculations of kaolinite using an empirical force field derived from high level Hartree–Fock calculations of octahedral aluminum clusters in combination with

a harmonic valence (bonded) force field developed previously for zeolites.<sup>25,28</sup> Although successful in reproducing the bulk structure of kaolinite, with all atoms free to translate, the Bougeard et al.<sup>21</sup> approach is limited to small-scale simulations of relatively well-known mineral structures, because of the large number of force field parameters needed to describe the bonded states. Sainz-Diaz et al.<sup>29</sup> developed a force field for the simulation of phyllosilicate phases based on interatomic potentials taken from previous aluminosilicate mineral models, and allowing for full atomic relaxation. Three-body bond bend terms were added to maintain the appropriate metal–oxygen coordination polyhedra geometry, and partial metal occupancies were used to describe disorder for metal substitutions in each structural sheet. The force field performs reasonably well in describing the structures of various medium and high charge phyllosilicates. However, difficulties arise for low charge phases such as pyrophyllite where relatively weak interactions occur across the interlayer region. Additionally, formal charges on metals and structural oxygens (non-hydroxyl) are utilized and may not be accurate for simulating sorption and other surface phenomena. As with the force field of Teppen et al.,<sup>22</sup> transferability remains a very important issue in the practical implementation of these alternative force field approaches.

Molecular modeling of real clay/solution interfaces often requires the description of complex and incompletely or poorly characterized crystal structures, low symmetries, large unit cells, variable compositions, and complex and variable interlayers and interfaces. The numerous parameters of a bonded force field are not easily transferred from relatively simple and well-known structures to systems with complex and ill-defined bond structures. For such systems, the application of a bonded force field is problematic because it can easily lead to significant overparametrization due to lack of the experimental data to constrain all the force field parameters necessary to describe bonded interactions.

In this paper we present an alternative approach to the development of a general force field for molecular simulations of hydrated crystalline compounds and their interfaces with fluid phases. CLAYFF is based on an ionic (nonbonded) description of the metal–oxygen interactions associated with hydrated phases. All atoms are represented as point charges and are allowed complete translational freedom within this force field framework. Metal–oxygen interactions are based on a simple Lennard-Jones (12-6) potential combined with electrostatics. The empirical parameters are optimized on the basis of known mineral structures, and partial atomic charges are derived from periodic DFT quantum chemical calculations of simple oxide, hydroxide, and oxyhydroxide model compounds with well-defined structures. Thus, in contrast to Teppen et al.<sup>22</sup> and Bougeard et al.,<sup>21</sup> we incorporated a set of experimental crystal structure refinements of these model phases to parametrize the empirical force field, rather than relying on quantum-mechanical calculations alone. Oxygen and hydroxyl charges vary depending on their occurrence in water molecules, hydroxyl groups, and bridging and substitution environments. The flexible SPC water model is used to describe the H<sub>2</sub>O and OH behavior. Harmonic terms are included to describe the bond stretch and bond angle bend terms associated with water molecules, hydroxyls, and dissolved polyatomic molecules and ions—the only type of bonded interactions explicitly defined in the force field.

The following section presents the details of the force field development and is followed by a section that describes its application to several classes of hydroxide, oxyhydroxide, and clay phases.

## Methods

CLAYFF is based on the single point charge (SPC) water model of Berendsen et al.<sup>30</sup> to represent the water, hydroxyl, and oxygen–oxygen interactions. This water model has been successfully used in a variety of molecular simulations to evaluate water structure and properties<sup>30–33</sup> and for the interaction of water with hydroxide mineral surfaces.<sup>34–36</sup> Compared to the more complex water models (e.g., TIP4P, BJH, etc.), the SPC is relatively simple in having partial charges centered directly on each of three atoms, and the short-range interactions represented by a simple Lennard-Jones term. Bond stretch and bond angle terms are introduced into the SPC water model using the expressions determined by Teleman et al.<sup>37</sup> to ensure full flexibility for the water and hydroxide components.

The total energy in a molecular mechanics simulation is determined by the evaluation of the appropriate energy term for every atom–atom interaction in the system. Generally, the total energy is expected to have contributions from the Coulombic (electrostatic) interactions, the short-range interactions (often referred to as the van der Waals term), and the bonded interactions:

$$E_{\text{total}} = E_{\text{Coul}} + E_{\text{VDW}} + E_{\text{bond stretch}} + E_{\text{angle bend}} \quad (1)$$

The bonded terms include the bond stretch and angle bend energy terms that are represented in the flexible SPC water model as harmonic terms. Coulombic and VDW interactions are excluded for proximate intramolecular (bonded) interactions (i.e., 1-2 and 1-3 atom position exclusions). Only intermolecular O–O and O–H nonbonded interactions (Coulombic and VDW terms) need to be evaluated in this case.

The Coulombic energy is represented by eq 2 where the energy of the interaction is inversely proportional to the distance of separation  $r_{ij}$ :

$$E_{\text{Coul}} = \frac{e^2}{4\pi\epsilon_0} \sum_{i \neq j} \frac{q_i q_j}{r_{ij}} \quad (2)$$

The partial charges  $q_i$  and  $q_j$  are derived from quantum mechanics calculations,  $e$  is the charge of the electron, and  $\epsilon_0$  is the dielectric permittivity of vacuum ( $8.85419 \times 10^{-12}$  F/m). The van der Waals energy term, represented by the conventional Lennard-Jones (12-6) function, includes the short-range repulsion associated with the increase in energy as two atoms approach each other and the attractive dispersion energy:

$$E_{\text{VDW}} = \sum_{i \neq j} D_{o,ij} \left[ \left( \frac{R_{o,ij}}{r_{ij}} \right)^{12} - 2 \left( \frac{R_{o,ij}}{r_{ij}} \right)^6 \right] \quad (3)$$

$D_{o,ij}$  and  $R_{o,ij}$  are empirical parameters derived from the fitting of the model to observed structural and physical property data. We used a large number of experimental structures for simple oxides, hydroxides, and oxyhydroxides to derive the optimal values for these parameters. The interaction parameters between the unlike atoms are calculated according to the arithmetic mean rule for the distance parameter,  $R_o$ , and the geometric mean rule for the energy parameter,  $D_o$ :

$$R_{o,ij} = \frac{1}{2}(R_{o,i} + R_{o,j}) \quad (4)$$

$$D_{o,ij} = \sqrt{D_{o,i} D_{o,j}} \quad (5)$$

In contrast to the covalent approach taken by Teppen et al.,<sup>22</sup>

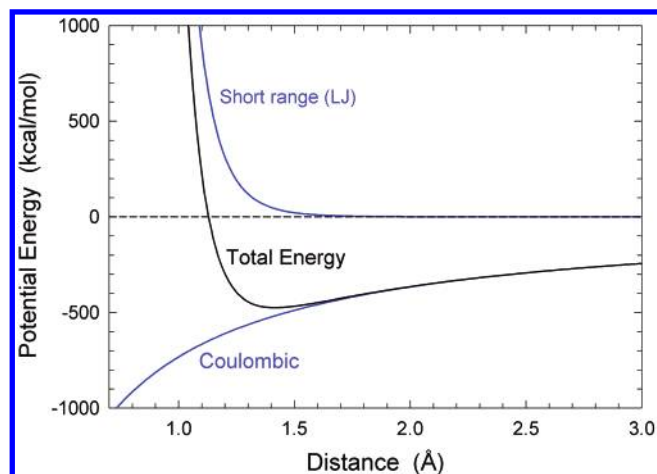
we incorporate an ionic description of the metal–oxygen interactions associated with the hydrated phases. This approach allows more flexibility in simulating complex and ill-defined crystal structures containing a large number of atoms and decreases the risk of overparametrization by drastically reducing the number of analytical expressions and force field parameters necessary to describe the energy of the atomic interactions throughout molecular mechanics simulations. The empirical parameters were optimized on the basis of the well-known structures of simple oxides, hydroxides, and oxyhydroxides. Partial charges were derived from periodic density functional theory calculations of these model compounds. Oxygen and hydroxyl charges can vary due to the occurrence in different structural environments.

Optimized values for the Lennard-Jones parameters were obtained using the General Utility Lattice Program GULP<sup>38</sup> computer program whereby the predicted structure of a model compound was fitted to the observed one using a Newton–Raphson method.<sup>39</sup> Lennard-Jones values identical to those for the SPC oxygen atom<sup>30</sup> were assigned to all oxygen atoms comprising the mineral lattice while partial charges were derived from electronic structure calculations for the simple oxides and hydroxides. Initially, the observed room-temperature structures for quartz ( $\alpha$ -SiO<sub>2</sub>),<sup>40</sup> corundum ( $\alpha$ -Al<sub>2</sub>O<sub>3</sub>),<sup>41</sup> boehmite ( $\gamma$ -AlO(OH)),<sup>42</sup> diaspore ( $\alpha$ -AlO(OH)),<sup>43</sup> and gibbsite ( $\gamma$ -Al(OH)<sub>3</sub>)<sup>44</sup> were used to derive the optimum Si–O and octahedral Al–O interaction values. The structure of kaolinite (Al<sub>2</sub>Si<sub>2</sub>O<sub>5</sub>(OH)<sub>4</sub>) derived by Bish<sup>2</sup> was later added to improve the number of observables to assist in the optimization of the Si–O interaction parameters. Aluminum and silicon values were initially derived to provide a modeling basis for more complex aluminosilicate structures such as clays derived by metal substitutions on this kaolinite framework.

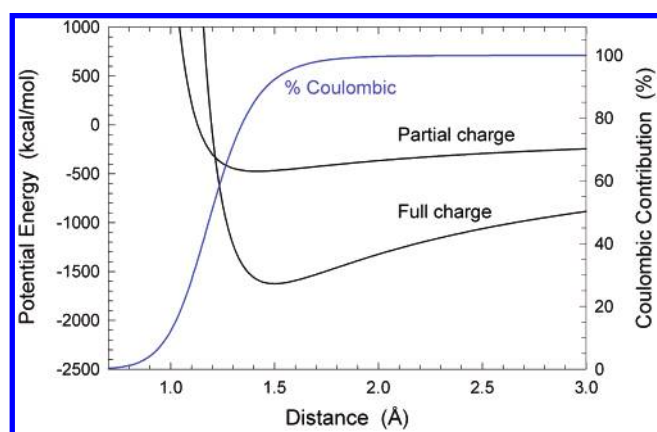
Partial charges were initially assigned on the basis of a combination of Mulliken<sup>45</sup> and electrostatic charge<sup>46,47</sup> determinations obtained from single point electronic structure calculations of the unit cells for the observed structures. The density functional method implemented in the quantum program DMol (Accelrys Inc., San Diego),<sup>48,49</sup> using the generalized gradient approximation<sup>50</sup> and a double numeric basis set including polarization functionals, was applied to examine the variation of charge with structure. Gas-phase cluster models for simple hydration states for silicon (e.g., Si(OH)<sub>4</sub>, Si(OH<sub>2</sub>)<sub>4</sub><sup>4+</sup>) and octahedral aluminum (e.g., Al(OH)<sub>6</sub><sup>3-</sup>, Al(OH<sub>2</sub>)<sub>6</sub><sup>3+</sup>) were optimized with DMol, and electron distributions analyzed to assist in the determination of optimal charges. Hydroxyl oxygens and hydrogens were assigned partial charges of  $-0.95$  and  $+0.425$ , respectively, in this fashion. Partial charges for water were maintained at the original SPC model values of Berendsen et al.<sup>30</sup>

Figure 1 provides an example of the behavior of potential energy as a function of interatomic distance for the case of a single tetrahedral silicon (st) and a bridging oxygen (ob) species. The total energy is composed of two nonbonded energy components: the electrostatic interaction represented by eq 2 and the short-range van der Waals energy represented by the Lennard-Jones eq 3. Because the attractive ( $1/r^6$ ) contribution to the last term is very small, the short-range component is almost entirely repulsive and provides a destabilizing positive energy while the long-range Coulombic interaction for the oppositely charged species is attractive and stabilizing. The combination of the two energy components results in a total energy curve characterized by an energy minimum at approximately 1.40 Å. In comparison, a complete lattice of inter-





**Figure 1.** Potential energy and its components for the tetrahedral silicon (st) and bridging oxygen (ob) interactions as a function of separation distance.



**Figure 2.** Comparison of total potential energy for the interaction of tetrahedral silicon (st) and bridging oxygen (ob) atom types compared to a similar force field based on full charges. The blue curve shows the contribution of the Coulombic energy to the total energy for the full charge case; a similar, but increasing, contribution occurs for the partial charge case.

acting st and ob species, as would occur in the simulation of crystalline quartz, would exhibit an energy minimum value shifted to about 1.61 Å as a result of the concerted interactions among all components.

The significance of using a partial charge model for CLAYFF is demonstrated in Figure 2 where the total potential energy for the interacting st–ob species is plotted as a function of distance for CLAYFF and a full charge force field (cvff\_aug; Accelrys Inc., San Diego). Both force fields provide similar equilibrium bond distances for the Si–O interaction but exhibit vastly different shapes for the potential well. The full charge force field introduces a stronger stabilizing influence to the interaction while the softer behavior associated with the CLAYFF model allows more flexibility and atomic motion; the vibrational behavior would be markedly different. While both force fields may be suitable simulating bulk structures, the full charge model will have artificially large Coulombic contributions that would strongly influence the interlayer structure and dynamics of clays and the sorption of species onto mineral surfaces.<sup>17</sup>

The parametrization procedure involves the evaluation of the total energy for each of the observed structures used in the fitting process based on some initial guess for the unknown metal–oxygen Lennard-Jones parameters. Phases containing hydroxyl groups require the evaluation of the stretch energy associated

with each of the O–H bonds. The bond stretch energy of the hydroxyl bond, like the O–H bond in SPC water, is described by a simple harmonic term:

$$E_{\text{bond stretch } ij} = k_1(r_{ij} - r_o)^2 \quad (6)$$

where  $k_1$  is a force constant and  $r_o$  represents the equilibrium bond length, both values taken from the flexible version of the SPC water model.<sup>37</sup> The bonded hydrogen associated with the hydroxyl group, like the hydrogens of SPC water, does not require any nonbonded Lennard-Jones component; only Coulombic interactions involving hydrogen charges are required. Intramolecular nonbonded interactions between oxygen and hydrogen in hydroxyl groups and water molecules are excluded due to the incorporation of the bonded terms. An Ewald summation is used to evaluate the long-range Coulombic energy to ensure proper convergence.<sup>51</sup> All partial charges, and bonded and nonbonded interaction parameters, were held fixed except for the metal–oxygen Lennard-Jones parameters that were allowed to vary during the parametrization.

Lennard-Jones values for octahedral iron were derived using the observed structures of goethite ( $\alpha\text{-FeO}(\text{OH})$ )<sup>52</sup> and lepidocrocite ( $\gamma\text{-FeO}(\text{OH})$ )<sup>42</sup> in the parametrization procedure. Similarly, the refinements for the structures of periclase ( $\text{MgO}$ )<sup>53</sup> and brucite ( $\text{Mg}(\text{OH})_2$ )<sup>54</sup> were used in the parametrization of the octahedral magnesium values, portlandite ( $\text{Ca}(\text{OH})_2$ )<sup>55</sup> was used to derive the octahedral calcium values, and  $\text{Li}_2\text{O}$ <sup>56</sup> was used in the parametrization for octahedral lithium. Partial charges were modified where necessary prior to the parametrization to be consistent with the desired stoichiometry expected for substitutions associated within clay sheets based on a pyrophyllite ( $\text{AlSi}_2\text{O}_5(\text{OH})$ ) model. Lennard-Jones parameters for tetrahedral aluminum, a common substitution in clay structures, were simply derived by using the same  $D_o$  and  $R_o$  values for tetrahedral silicon; the partial charge remained the same as that for octahedral aluminum. Additional parametrizations were performed to accommodate non-silicate layered structures requiring different partial charge assignments for the metal ions, such as magnesium and calcium in the simple hydroxides brucite and portlandite, respectively.

The nonbonded interaction parameters for CLAYFF are provided in Table 1. The corresponding CLAYFF bonded parameters for the water and hydroxyl interactions are listed in Table 2. The nonbonded Lennard-Jones parameters are presented in terms of a single atomic species type derived by the use of combination rules.<sup>57</sup> Combination rules allow Lennard-Jones parameters for single atom species to be combined in one of several ways to avoid the explicit definition for every possible atom–atom interaction in a simulation. We incorporate in CLAYFF the arithmetic mean rule for the  $R_o$  term (eq 4) and a geometric mean for the  $D_o$  parameters (eq 5), following the convention used in previous force fields.<sup>58</sup> This approach allows us to obtain parameters for single atom species from homogeneous atom pairs, such as for bridging oxygens from ob–ob interactions, and then derive parameters for atom species from corresponding heterogeneous atom pairs where one of the species has parameters determined as above. For example, parameters for tetrahedral silicon can be derived from those of the st–ob interactions when the ob values are known. Table 1 also includes nonbonded parameters for several aqueous species that are compatible with the SPC-type water model and which were obtained from the literature.<sup>32,59–61</sup> Parameters for aqueous cations derived for SPC and the extended SPC/E<sup>31</sup> version are included; the slight difference in charge between the two water

**TABLE 1: Nonbond Parameters for the CLAYFF Force Field**

species	symbol	charge (e)	$D_o$ (kcal/mol)	$R_o$ (Å)
water hydrogen	h*	0.4100		
hydroxyl hydrogen	ho	0.4250		
water oxygen	o*	-0.8200	0.1554	3.5532
hydroxyl oxygen	oh	-0.9500	0.1554	3.5532
bridging oxygen	ob	-1.0500	0.1554	3.5532
bridging oxygen with octahedral substitution	obos	-1.1808	0.1554	3.5532
bridging oxygen with tetrahedral substitution	obts	-1.1688	0.1554	3.5532
bridging oxygen with double substitution	obss	-1.2996	0.1554	3.5532
hydroxyl oxygen with substitution	ohs	-1.0808	0.1554	3.5532
tetrahedral silicon	st	2.1000	$1.8405 \times 10^{-6}$	3.7064
octahedral aluminum	ao	1.5750	$1.3298 \times 10^{-6}$	4.7943
tetrahedral aluminum	at	1.5750	$1.8405 \times 10^{-6}$	3.7064
octahedral magnesium	mgo	1.3600	$9.0298 \times 10^{-7}$	5.9090
hydroxide magnesium	mgh	1.0500	$9.0298 \times 10^{-7}$	5.9090
octahedral calcium	cao	1.3600	$5.0298 \times 10^{-6}$	6.2484
hydroxide calcium	cah	1.0500	$5.0298 \times 10^{-6}$	6.2428
octahedral iron	feo	1.5750	$9.0298 \times 10^{-6}$	5.5070
octahedral lithium	lio	0.5250	$9.0298 \times 10^{-6}$	4.7257
aqueous sodium ion <sup>a</sup>	Na	1.0	0.1301	2.6378
aqueous potassium ion <sup>b</sup>	K	1.0	0.1000	3.7423
aqueous cesium ion <sup>c</sup>	Cs	1.0	0.1000	4.3002
aqueous calcium ion <sup>b</sup>	Ca	2.0	0.1000	3.2237
aqueous barium ion <sup>d</sup>	Ba	2.0	0.0470	4.2840
aqueous chloride ion <sup>a</sup>	Cl	-1.0	0.1001	4.9388

<sup>a</sup> Smith and Dang.<sup>32</sup> <sup>b</sup> Koneshan et al.<sup>60</sup> <sup>c</sup> Smith and Dang.<sup>59</sup>  
<sup>d</sup> Åqvist.<sup>61</sup>

**TABLE 2: Bond Parameters for the CLAYFF Force Field**

bond stretch			$k_1$ (kcal/mol Å <sup>2</sup> )	$r_o$ (Å)
species $i$	species $j$			
o*	h*		554.1349	1.0000
oh	ho		554.1349	1.0000
ohs	ho		554.1349	1.0000
angle bend				
species $i$	species $j$	species $k$	$k_2$ (kcal/mol rad <sup>2</sup> )	$\theta_o$ (deg)
h*	o*	h*	45.7696	109.47
Metal	oh	ho	30.0	109.47
Metal	ohs	ho	30.0	109.47

models does not significantly affect the transferability of CLAYFF. The inclusion of these species in CLAYFF is important for the simulation of interlayer cations in clays and the analysis of the dynamic behavior of various solvated complexes on the external surfaces of minerals.

Delocalization of charges with the isomorphic substitution of a metal onto the octahedral or tetrahedral sheet of a clay is problematic when it comes to performing accurate molecular simulations. In particular, the metal substitution often leads to local charge imbalance (e.g., aluminum substitution for silicon in the tetrahedral sheet of a smectite clay) that can influence the structure and sorption properties of the interlayer and external surfaces of the clay.<sup>62,63</sup> CLAYFF accommodates this smearing of charge about a substitution site by assigning modified charges to the nearest neighbor oxygens associated with the substituting metal. The variation of partial charges for these oxygens was determined by performing a set of single point periodic DFT calculations using DMol for structures derived from the dioctahedral clay pyrophyllite.<sup>64</sup> Each clay model included the appropriate number of sodium counterions positioned along the midplane of an expanded interlayer region;

no interlayer waters were present. Single octahedral and double octahedral magnesium substitutions, tetrahedral aluminum substitution, and positional variation of each of these substitutions were investigated. We used periodic density functional theory<sup>48,49</sup> and the generalized gradient approximation<sup>50</sup> with a double numeric basis set including polarization functionals to examine the electronic structure for each clay model. Mulliken population analysis of the resulting electron densities was used to evaluate the delocalization of charge as a function of substitution site, and when the Mulliken population analysis was combined with constraints on stoichiometry and cell neutrality, we derived a self-consistent set of partial charges that are compatible with the Lennard-Jones parameters in Table 1. Oxygen partial charges vary from -0.95 for the hydroxyl oxygen (oh), to -1.05 for a bridging oxygen (ob), to -1.1688 for a bridging oxygen coordinated to tetrahedral substituted sites (obts), to -1.2996 for a bridging oxygen coordinated to two octahedral substitutions or tetrahedral-octahedral substitutions (obss). The term bridging oxygen is used loosely in this discussion to represent an edge-sharing polyhedra oxygen that is not part of a hydroxyl group. Trioctahedral layered silicates (e.g., talc, vermiculite, and phlogopite) are necessarily described by obts, obss, and ohs oxygen types due to the substitution of the complete octahedral layer by divalent metal ions, including vacancies associated with dioctahedral structures.

An additional enhancement of CLAYFF that was incorporated to better describe metal sorption on hydrated surfaces, and to improve the vibrational (librational) behavior of hydroxyl groups, is the inclusion of an angle bend (three-body) term for describing hydroxyl groups. The energy of the angle bend term can be described by a simple harmonic relationship:

$$E_{\text{angle bend } ijk} = k_2(\theta_{ijk} - \theta_o)^2 \quad (7)$$

where  $k_2$  is a force constant,  $\theta_{ijk}$  is the bond angle for the metal-oxygen-hydrogen, and  $\theta_o$  represents the equilibrium bond angle. Equation 7 is equivalent to the flexible bond angle component associated with the modified SPC water model.<sup>37</sup> Optimum values for  $k_2$  and  $\theta_{ijk}$  (see Table 2) were determined through an iterative process by comparing the results of molecular simulations of the structure and infrared spectra for gibbsite and portlandite with the observed frequencies from Farmer.<sup>65</sup> In practice, the three-body energy function was incorporated into CLAYFF as a modified Stillinger-Weber function with parameters chosen to reproduce the harmonic behavior of eq 7 over the expected variation of metal-hydroxyl bend angles. Although helpful in describing surface hydroxyl behavior, the functionality and implementation were difficult and computationally expensive to apply. Relatively small time steps (0.0005 ps) were required for stability and considerable computational effort was needed to account for all appropriate metal-hydroxide interactions. We consider the three-body term for surface hydroxyls an optional feature of CLAYFF and therefore do not include it in the molecular simulations of the bulk structures discussed below.

All molecular simulations presented here were completed using the Open Force Field (OFF) module within the Cerius<sup>2</sup> molecular modeling interface (Accelrys Inc., San Diego). Molecular models of each structure were generated on the basis of recently published crystal structure refinements, with particular emphasis on those structures determined from neutron data and having well-characterized hydrogen positions. The total potential energy of the unit cell structure, or a structure based on a related supercell, was calculated using eq 1 with the energy terms for nonbonded (eqs 2 and 3) and bonded (eqs 6 and 7)

**TABLE 3: Summary of Structural Properties Derived from Molecular Dynamics Simulations of Boehmite, Portlandite, Kaolinite, and Pyrophyllite**

	boehmite $\gamma$ -AlO(OH)		portlandite Ca(OH) <sub>2</sub>		kaolinite Al <sub>2</sub> Si <sub>2</sub> O <sub>5</sub> (OH) <sub>4</sub>		pyrophyllite AlSi <sub>2</sub> O <sub>5</sub> (OH)	
	simulation	observed <sup>d</sup>	simulation	observed <sup>b</sup>	simulation	observed <sup>c</sup>	simulation	observed <sup>d</sup>
Cell Structure								
<i>a</i> axis (Å)	2.980 ± 0.015	2.876	3.693 ± 0.044	3.589	5.190 ± 0.05	5.154	5.192 ± 0.034	5.160
<i>b</i> axis (Å)	12.442 ± 0.061	12.240	3.694 ± 0.040	3.589	8.956 ± 0.087	8.942	9.021 ± 0.061	8.966
<i>c</i> axis (Å)	3.732 ± 0.018	3.709	4.796 ± 0.061	4.911	7.361 ± 0.074	7.391	9.459 ± 0.163	9.347
$\alpha$ angle (deg)	90.01 ± 0.39	90.0	82.04 ± 1.25	90.0	90.77 ± 1.81	91.92	91.38 ± 0.87	91.18
$\beta$ angle (deg)	90.00 ± 0.16	90.0	97.99 ± 1.21	90.0	104.17 ± 0.81	105.05	98.97 ± 1.90	100.46
$\gamma$ angle (deg)	90.04 ± 0.72	90.0	121.59 ± 0.91	120.0	90.40 ± 0.49	89.8	89.81 ± 0.45	89.64
density (g/cm <sup>3</sup> )	2.881 ± 0.018	3.052	2.239 ± 0.032	2.246	2.579 ± 0.048	2.608	2.738 ± 0.049	2.815
basal <i>d</i> spacing (Å)	6.180 ± 0.030	6.120	4.734 ± 0.062	4.911	7.157 ± 0.109	7.133	9.333 ± 0.160	9.190
Bond Distance (Å)								
O–H	1.034 ± 0.024	0.928	1.023 ± 0.021	0.942	1.011 ± 0.009	0.978	1.106 ± 0.002	0.978
Al–OH	1.943 ± 0.071	1.902			1.999 ± 0.092	1.888	1.959 ± 0.098	1.897
Al–O	1.992 ± 0.121	1.918			1.993 ± 0.093	1.924	2.056 ± 0.159	1.927
Si–O <sub>basal</sub>					1.565 ± 0.031	1.613	1.580 ± 0.033	1.615
Si–O <sub>apical</sub>					1.633 ± 0.045	1.633	1.578 ± 0.036	1.614
Ca–OH			2.515 ± 0.119	2.369				

<sup>a</sup> Christensen et al.<sup>42</sup> <sup>b</sup> Desgranges et al.<sup>55</sup> <sup>c</sup> Bish.<sup>2</sup> <sup>d</sup> Lee and Gugenheim.<sup>64</sup>

interactions defined by CLAYFF, as appropriate for the hydration state of the material. The long-range Coulombic interactions were calculated using the standard Ewald summation method<sup>51</sup> with the refinement of Karasawa and Goddard<sup>66</sup> to increase the efficiency of convergence. A “spline cutoff” method, operating between atom–atom distances of 8.0 and 8.5 Å, was used to evaluate the non-Coulombic interactions to preserve a continuous transition to zero energy with distance.

Energy-optimized structures were obtained using a smart minimizer approach that combines a steepest descent method with several modified Newton–Raphson algorithms<sup>67</sup> to ensure proper convergence. Simulation cells were typically converted to the *P1* triclinic space group symmetry allowing all crystallographic cell parameters (*a*, *b*, *c*,  $\alpha$ ,  $\beta$ , and  $\gamma$ ) and atom positions to vary during the optimization and dynamics simulations—CLAYFF allows complete flexibility in allowing all atoms and cell parameters to be unconstrained. Energy-minimized models were used as initial structures for molecular dynamics simulations that were performed as *NPT* canonical ensembles at *P* = 0.1 MPa and *T* = 300 K, using the Parinello–Rahman<sup>68</sup> method with the Verlet<sup>69</sup> algorithm for integration of the equations of motion. A time step of 0.001 ps was used in all of MD runs. Each system was allowed to relax and equilibrate for 100 ps of MD simulation. To ensure thermodynamic equilibrium, the convergence of total energy and its components (kinetic and potential; Coulomb, non-Coulomb, bonding, etc.) as well as temperature, density, and atomic radial distribution functions were carefully monitored during this equilibration period. Usually, CLAYFF provides relatively fast equilibration for the MD simulation of hydrated systems, typically within less than 20 ps. Following the equilibration, the equilibrium dynamic trajectory was recorded during the next 40–100 ps of MD simulation at 0.004 ps intervals for the statistical analysis of the structural and dynamical properties of the simulated system.

## Results and Discussion

The CLAYFF force field was used to simulate the structure of a variety of model hydroxide, oxyhydroxide, and clay phases following the procedures noted above. Energy-minimized structures and those obtained from MD simulations are presented. Table 3 provides a summary of the resulting cell parameters and bond distances and a comparison with the

experimental values. In addition to the structures presented in this paper, and those structures from the data set used in the parametrization, CLAYFF was also tested on a variety of different crystalline compounds throughout the course of the parametrization. Mostly this was to ascertain the general applicability of the force field to unique crystal structures and bonding environments. Energy minimizations provided a relatively fast means of checking the suitability of the parameters in predicting coordination polyhedra, bond lengths and angles, cell parameters, and density of these phases. Included among the investigated phases are sillimanite, spodumene, goethite, illite, talc, antigorite, beidellite, vermiculite, and hydrocalumite. The results of these simulations will be presented in future journal articles.

**Boehmite and Portlandite.** The energy-minimized structures of an oxyhydroxide phase, boehmite, and hydroxide phase, portlandite, are presented in Figures 3 and 4. Although both phases are part of the data set of model structures used in the parametrization procedure (metal–oxygen parameters only), they provide good examples of layered structures that are controlled in part by H-bonding. The boehmite unit cell presented in Figure 3 exhibits the directional hydrogen bonds extending across the interlayer region with the coordination of the hydroxyl hydrogen with the opposing hydroxyl oxygen. The supercell of the portlandite structure shown in Figure 4 indicates a similar hydrogen bonding across the aluminum octahedra layers; however, the H-bonding is directional and normal to the *ab*-plane normal to the presented view. Results of the MD simulations on supercell representations (nine unit cells) of each structure indicate the hydrogen bonding exists between paired hydrogens and oxygens throughout the 100 ps of simulation time. Librational motions of the Al–O–H and Ca–O–H bond angle occur in a concerted fashion among the interlayer hydroxyls while still preserving the directionality of H-bonds.

**Kaolinite and Pyrophyllite.** Two dioctahedral aluminosilicate clay structures, kaolinite and pyrophyllite, were successfully simulated using CLAYFF. The energy-optimized structures are presented in Figures 5 and 6. Kaolinite is a 1:1 layer clay composed of a repeating layer of an aluminum octahedral (O) sheet and a silicon tetrahedral (T) sheet. Interlayer hydroxyl groups extend from the octahedral sheet into the interlayer region where they form hydrogen bonds to basal oxygens of the opposing tetrahedral silicate sheet. Inner hydroxyl groups occur



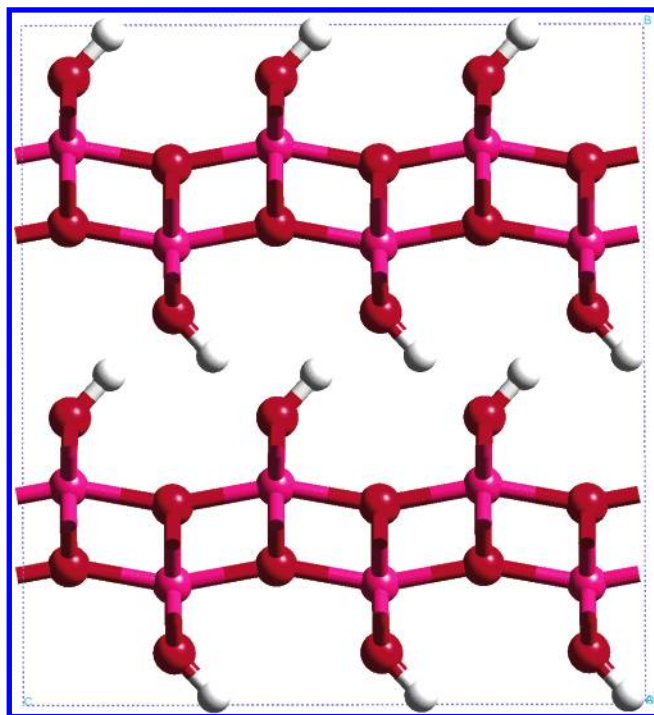


**Figure 3.** Energy minimized structure of boehmite ( $\gamma$ -AlOOH) based on a unit cell structural optimization. A supercell composed of three unit cells is presented here to provide a better representation of the crystal structure. Projection view along the [100] direction.

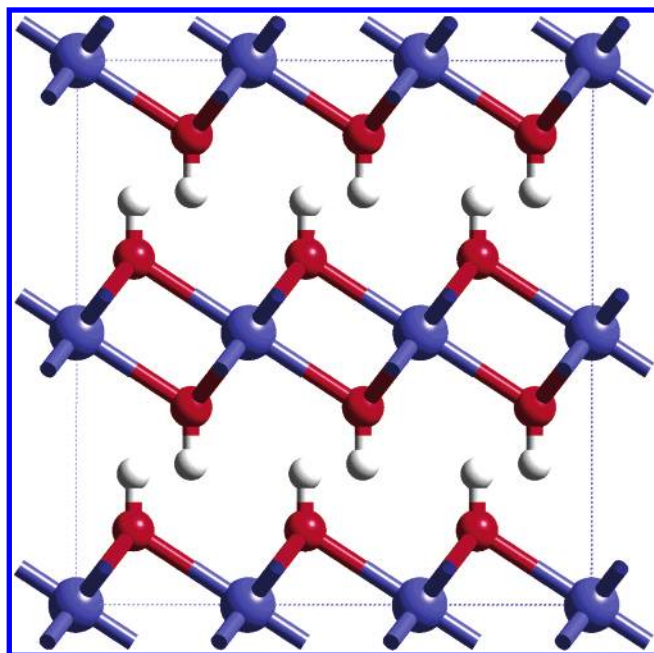


**Figure 4.** Energy minimized structure of portlandite ( $\text{Ca}(\text{OH})_2$ ) based on a unit cell structural optimization. A supercell composed of six unit cells is presented here to provide a better representation of the crystal structure. Projection view along the [010] direction.

between the sheets extending from the aluminum octahedra and are directionally influenced by the octahedral vacancy. The observed structure of kaolinite derived from a refinement of neutron diffraction data<sup>2</sup> is reproduced by the energy minimized structure of the unit cell. Results of the molecular dynamics simulation are presented in Table 3. The critical hydrogen bonding is exhibited for both interlayer and inner hydroxyl groups, although the interlayer distances are shortened by 10%. Noteworthy of the CLAYFF simulation of kaolinite is that all three crystallographically unique interlayer hydroxyl groups are

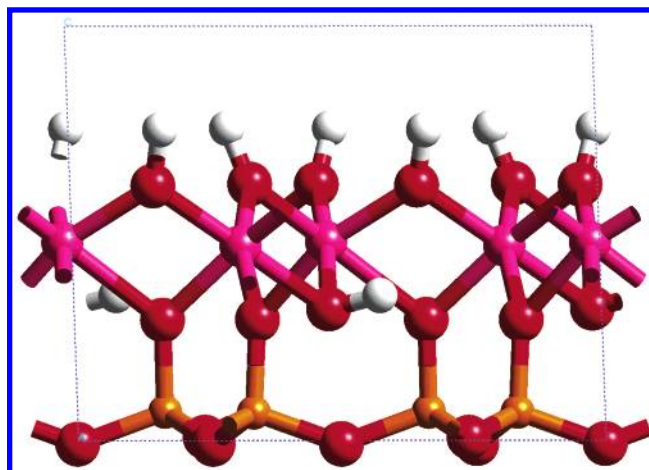


**Figure 5.** Energy minimized structure of kaolinite ( $\text{Al}_2\text{Si}_2\text{O}_5(\text{OH})_4$ ) based on a unit cell structural optimization. Projection view along the [100] direction.

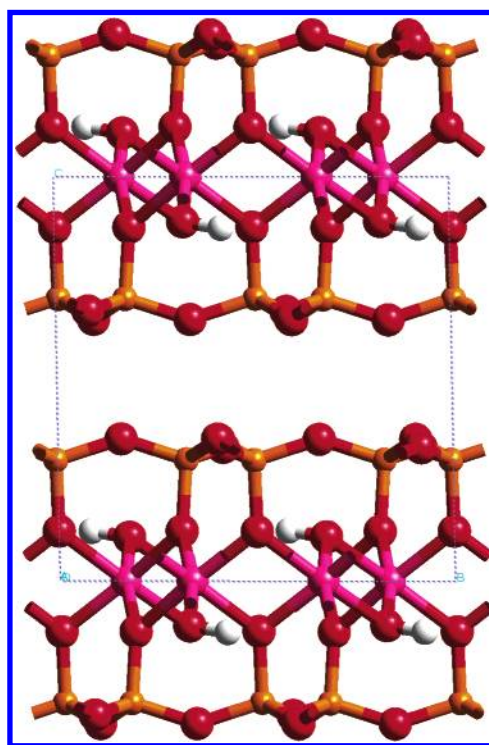


**Figure 6.** Energy minimized structure of pyrophyllite ( $\text{Al}_2\text{Si}_4\text{O}_{10}(\text{OH})_2$ ) based on a unit cell structural optimization. Projection view along the [100] direction.

actively involved in the interlayer H-bonding, in agreement with observation, in contrast to results obtained using the bonded force field of Teppen et al.<sup>22</sup>

Pyrophyllite is a 2:1 layer clay composed of repeating TOT layers. The interlayer region is bounded by two opposing tetrahedral sheets, which are coordinating through weak van der Waals interactions. The energy-minimized structure and that obtained by molecular dynamics are both in agreement with the X-ray diffraction refinement of Lee and Guggenheim.<sup>64</sup> A comparison of the structures is presented in Table 3. No neutron diffraction study of pyrophyllite has been published; therefore little structural information on the disposition of the hydroxyl groups is known. The molecular model, however, provides an opportunity to determine the most probable hydrogen positions and assess their dynamical behavior. The energy-optimized structure for the pyrophyllite unit cell presented in Figure 6 indicates that the hydroxyls are disposed subparallel to the *ab*-

plane with the hydrogen directed toward the octahedral vacancy. Simulations of trioctahedral clays, such as talc and vermiculite, indicate that the hydroxyls are directed subparallel to the *c*-axis and are locally influenced by tetrahedral substitutions and interlayer species.

**Montmorillonite.** The more complex chemistry and structure of the clay montmorillonite can be simulated using CLAYFF. Montmorillonite, a dioctahedral smectite clay with monoclinic symmetry, is characterized by magnesium substitution for aluminum in the octahedral sheet with some aluminum substitution for silicon in the tetrahedral sheet. The substitutions generate a net negative charge on the clay TOT layer that is balanced by the incorporation of metal cations into the interlayer region. Water molecules typically solvate the interlayer cations, and additional waters can be incorporated depending upon the ambient humidity. Using pyrophyllite as the basis for the dioctahedral structure,<sup>64</sup> a montmorillonite model was created that corresponded to the observed montmorillonite compositions typical for a sodium smectite clay.<sup>70</sup> Due to the lack of single crystals of montmorillonite and the extensive stacking disorder associated with smectites—therefore making X-ray structural refinements quite difficult if not impossible—the molecular modeling provides an opportunity for obtaining a realistic structural model.<sup>71</sup> A supercell composed of four unit cells and having the composition of  $\text{Na}_3(\text{Si}_{31}\text{Al})(\text{Al}_{14}\text{Mg}_2)\text{O}_{80}(\text{OH})_{16} \cdot n\text{H}_2\text{O}$  was used to model montmorillonite in a series of lattice energy and molecular dynamics simulations. The most favorable sites for magnesium substitution in the octahedral sheet were first identified relative to the single tetrahedral aluminum substitution using static energy determinations with CLAYFF. The optimum configuration was then used as a basis for evaluating the equilibrium structure as a function of water content.

MD simulations were performed to examine the swelling behavior of montmorillonite. Individual water molecules were added incrementally to the interlayer region of the simulation cell, with the creation of each new hydration state being followed by a molecular dynamics simulation performed as a canonical *NPT*-ensemble for 30 ps. This equilibration run was followed by an additional 20 ps of simulation during which the cell parameters were monitored to derive mean values and for obtaining the mean equilibrated basal plane (001) *d*-spacing. Single water molecules were initially introduced into the simulation cell up to a configuration having 23  $\text{H}_2\text{O}$  molecules. Continued swelling of the montmorillonite was performed by introducing two water molecules for each simulation up to a maximum of 99 water molecules per simulation cell. An additional series of simulations were completed by deswelling the montmorillonite by incrementally removing two water molecules per step starting with the 99 water configuration. Uncertainties in the basal *d*-spacing were derived as one standard deviation values from the statistical analysis of the dynamics trajectories.

Figure 8 presents the results of the series of simulations for the hydration of montmorillonite in the form of the swelling curve where only the results for the first 59 water molecules shown. The calculated basal (001) *d*-spacing for the clay is plotted as a function of water content along with the experimental data obtained by Fu et al.<sup>72</sup> The model results are in very good agreement with experiment and exhibit the expansion of the clay through two clearly-defined expanded layer structures. Additionally, the fine structure of the swelling curve is reproduced as water molecules first expand the clay layers and then fill in voids about the sodium ions and other waters. The

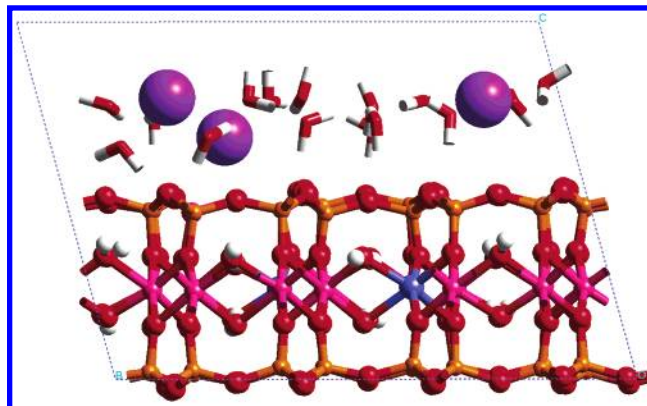


**Figure 7.** Snapshot of the equilibrium structure of a Na-montmorillonite ( $\text{Na}_3(\text{Si}_{31}\text{Al})(\text{Al}_{14}\text{Mg}_2)\text{O}_{80}(\text{OH})_{16} \cdot 16\text{H}_2\text{O}$ ) based on an *NPT* molecular dynamics simulation at 300 K and 1 bar. The octahedral sheet includes magnesium substitutions (blue atoms) and the tetrahedral sheet contains aluminum substitutions (pink atoms, partially obscured). The large purple spheres are interlayer sodium ions surrounded by water molecules that are represented as bent cylinders. Hydroxyl groups are shown as bonded white and red atoms angled from the corners of the octahedra. Projection view along the [100] direction.

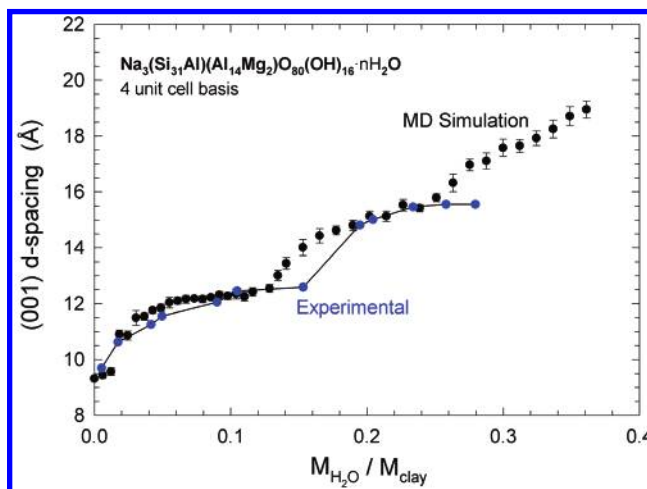


**Figure 8.** Swelling curve for the hydration of Na-montmorillonite derived from equilibrated molecular dynamics simulations. Experimental data (blue symbols) from Fu et al.<sup>72</sup>

model results are in general agreement with previous theoretical swelling curves for smectite clays derived using rigid water and clay structures,<sup>15,73,74</sup> and provide further refinements by incorporating a fully flexible force field. This latter effect is manifested in a slightly more confined interlayer region for a given water content as the water relaxes in solvating both the clay surface and interlayer cations.

Smectite clays, like montmorillonite, expand with the introduction of water into the interlayer region by reducing the electrostatic interactions of the negatively charged layers while simultaneously solvating the free sodium ions and clay surface. The total energy is further reduced with the addition of more water molecules that leads to the development of a hydrogen-bonded network of water within the interlayer. This configuration corresponds to a montmorillonite having a basal spacing of 12 Å, a stable single-layer hydrate. The additional backfill of waters in the void space of the single-layer hydrate leads to further stabilization until the water content is at a critical level where the montmorillonite expands to approximately 15 Å with the formation of a stable two-layer hydrate. The two-layer hydrate is observed in nature and represents the limit of the clay expansion under most ambient conditions<sup>72</sup>—the experi-



mental curve in Figure 8 levels off at approximately 15 Å. However, the molecular modeling approach allows for further analysis by a continuation of the clay swelling with the addition of more water molecules, well beyond equilibrium conditions. The swelling curve of Figure 8 hints at the existence of a three-layer hydrate, represented by a shoulder at approximately 0.3 g of H<sub>2</sub>O/g of clay. However, with further addition of water the montmorillonite expands without leveling off at a stable multilayered water configuration. At this point, the clay has expanded to where the electrostatic interactions of the TOT layers are effectively shielded from the sodium ions by the interlayer water, and there is no effective coordinated stabilization of the configuration. In other words, the energy of the system is now dominated by the hydrogen bonding of the large number of interlayer waters such that this region is more representative of bulk water than interlayer water. The series of deswelling simulations provided identical montmorillonite structures and basal *d*-spacings, within the associated standard deviation, as observed for the series of swelling simulations. This lack of hydration–dehydration hysteresis supports the attainment of fully equilibrated montmorillonite structures with the simulations.

As originally reported by Teppen et al.,<sup>22</sup> we observe a similar translational shift of neighboring layers along the basal planes during the molecular dynamics simulation of phyllosilicates, especially for those characterized by weak interlayer interactions. This shearing effect is more pronounced with the incorporation of interlayer water molecules, as in the above examples for the swelling of a smectite clay. Molecular dynamics trajectories often exhibit a systematically changing values for the  $\alpha$  and  $\gamma$  cell parameters as the simulation cell distorts with simulation time. Due to periodic nature of the simulations, the equilibrated structures and associated basal *d*-spacings provide an accurate representation of the phyllosilicate. The registry shift of the clay layers presumably is related to the evolving velocities of the atoms of the interlayer species and the relatively weak restoring forces.

**Hydrotalcite.** A final example of the success of the CLAYFF force field is provided for the case of hydrotalcite, one of the so-called anionic clays. These materials, also referred to as layered double hydroxides (LDH), are an important class of natural and synthetic materials that have significant anion-exchange and sorption properties.<sup>75–77</sup> Hydrotalcite consists of single sheets of brucite Mg(OH)<sub>2</sub>, with octahedrally coordinated magnesium ions, alternating with interlayer regions composed of water and various anions. In contrast to regular clay phases, hydrotalcite has a permanent positive charge residing on the hydroxide layer as a result of aluminum substituting for magnesium. The structure of the interlayer and surface regions of hydrotalcite is unknown due to the difficulty in X-ray determinations for a material with structural disorder and significantly small grain size. Although nuclear magnetic resonance methods have shown promise in determining the disposition of anions and water in the interlayer and surfaces of hydrotalcite,<sup>78</sup> much of our understanding of the interlayer structure and dynamics results from molecular simulations. Most of this theoretical effort has examined the behavior of interlayer anions and hydration<sup>34–36,79–82</sup> and the intercalation of organic molecules.<sup>83,84</sup>

A series of molecular dynamics simulations of the structure and hydration of hydrotalcite using CLAYFF was performed by Wang et al.<sup>79</sup> The composition of the hydrotalcite corresponded to Mg<sub>2</sub>Al(OH)<sub>6</sub>Cl·*n*H<sub>2</sub>O with chloride representing the interlayer anions. This stoichiometry results in an interlayer

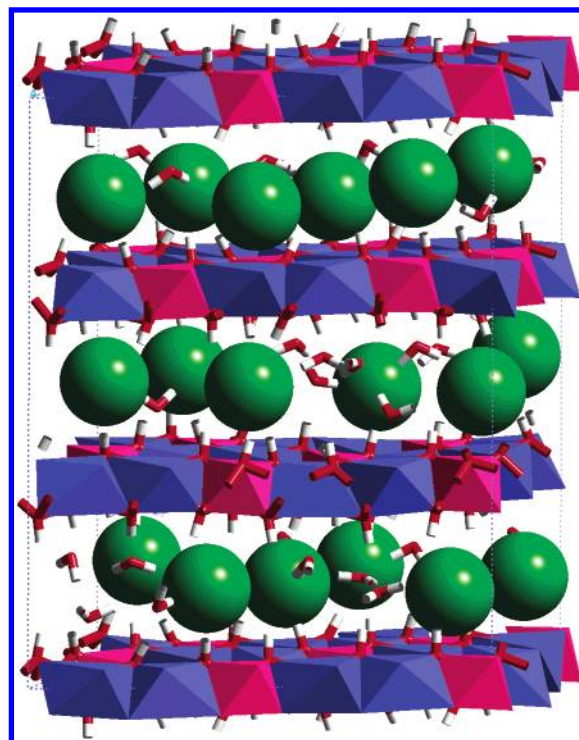


**Figure 9.** Snapshot of the equilibrium structure of hydrotalcite (Mg<sub>2</sub>Al(OH)<sub>6</sub>Cl·2H<sub>2</sub>O) derived from an *NPT* molecular dynamics simulation at 300 K and 1 bar from Wang et al.<sup>79</sup> The simulation cell is composed of 18 crystallographic unit cells. The blue polyhedra represent octahedral magnesium and the pink ones indicate aluminum octahedra. The green spheres represent interlayer chloride ions with water molecules represented by bent cylinders. Oblique view slightly offset from the [100] direction.

with a single chloride ion per aluminum with variable water solvating the chloride ion. The initial structure was based on the refinement of Bellotto et al.<sup>85</sup> derived from powder X-ray diffraction data. The original rhombohedral unit cell was expanded to a 6 × 3 × 1 supercell maintaining long-range Mg–Al ordering in the hydroxide layers. The MD simulations were performed with no symmetry constraints beyond the periodic boundary conditions for the supercell (i.e., *P1* symmetry). In contrast to previous simulation studies of magnesium–aluminum hydrotalcite, all lattice parameters and atom positions were unconstrained during the *NPT*-ensemble simulations. Similar conditions for the MD runs as described above were used in these simulations. However, the structure presented here resulted from a 100 ps simulation, although equilibration usually occurred within the first 20 ps.

A snapshot of the equilibrated structure of hydrotalcite with composition Mg<sub>2</sub>Al(OH)<sub>6</sub>Cl·2H<sub>2</sub>O is provided in Figure 9. For this composition each chloride ion is coordinated by two water molecules, leading to a complete single hydration layer in each interlayer region. While the aluminum occurs in regular polyhedra, the magnesium form distorted octahedra, with half the magnesium atoms being shifted either up or down from the midplane of the hydroxide layer. Either water or chloride coordinates to the magnesium creating a seven-coordinated polyhedron.<sup>79</sup> Additionally, the hydroxyl groups associated with the hydroxide layers coordinate above and below to the interlayer chloride to form a stable coordination environment within the interlayer.

As with normal clays, hydrotalcite expands along the *c*-axis to accommodate the hydration process. The structure for the composition shown here has a *c*-axis dimension of 23.9 Å and is in good agreement the 23.6 Å value that has been obtained

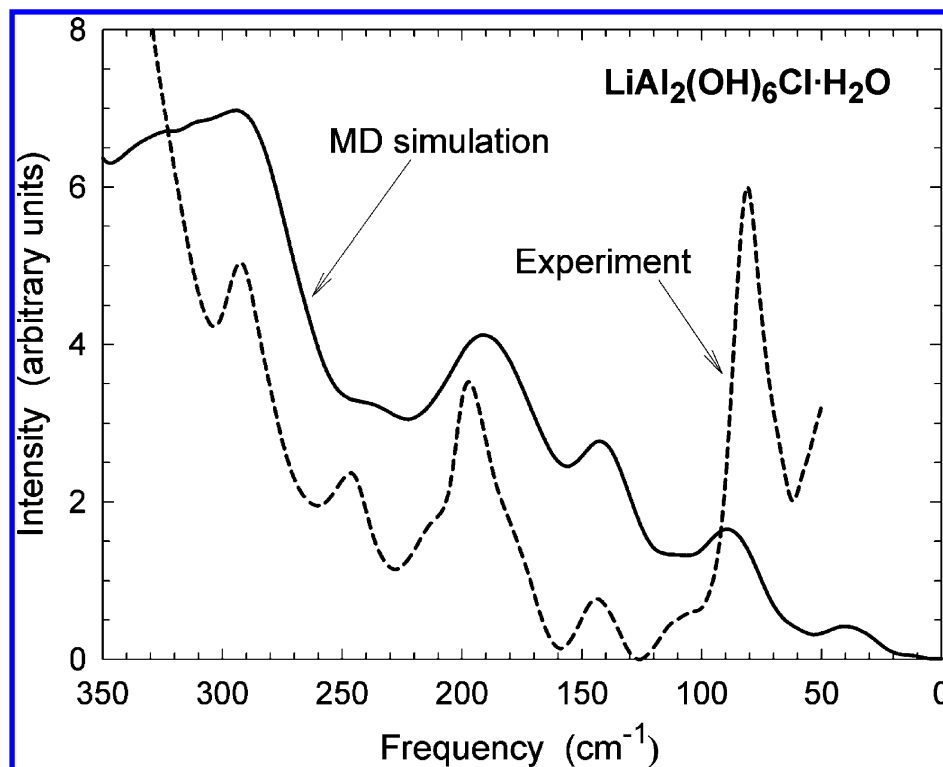


**Figure 10.** Comparison of calculated power spectra for  $\text{LiAl}_2(\text{OH})_6\text{Cl}\cdot\text{H}_2\text{O}$  hydrotalcite (solid line) with observed far infrared spectra (dashed line). See Kirkpatrick et al.<sup>89</sup> for the details of experimental and computational methods.

by X-ray diffraction studies for the maximum swelling of hydrotalcite under ambient conditions.<sup>86,87</sup> Wang et al.<sup>79</sup> determined a complete swelling curve for hydrotalcite that, in addition to two stable hydration states (*c*-axis dimensions of 21.7 Å and 23.9 Å), includes a complete second layer hydration of the interlayer occurring at a *c*-axis dimension of 31.8 Å. Also, recent molecular simulation studies of other LDH phases,  $\text{Mg}_3\text{-Al}(\text{OH})_8\text{Cl}\cdot 3\text{H}_2\text{O}$  and  $\text{LiAl}_2(\text{OH})_6\text{Cl}\cdot\text{H}_2\text{O}$ , as well as cement-related hydrated Ca-aluminate and Ca-silicate phases hydrocalumite  $\text{Ca}_2\text{Al}(\text{OH})_6\text{Cl}\cdot 2\text{H}_2\text{O}$ , ettringite  $\text{Ca}_6[\text{Al}(\text{OH})_6]_2[\text{SO}_4]_3\cdot 26\text{H}_2\text{O}$ , and tobermorite  $\text{Ca}_5\text{Si}_6\text{O}_{16}(\text{OH})_2$ , successfully used CLAYFF to determine the structure and dynamics of interlayer and surface species.<sup>34,36,80,81</sup>

**Vibrational Spectra.** Vibrational spectroscopy, including Raman and infrared measurements, plays a considerable role in the molecular-level understanding of the structure and dynamics of clays and clay-related materials.<sup>88</sup> However, the interpretation of experimental spectral features related to interlayer and surface environments of these materials is often difficult due to compositional complexity, structural disorder, and the wide range of complicated and typically low-frequency motions that contribute to the observed spectra. In contrast to the relatively simple metal–oxygen (M–O) and O–H stretching, and M–O–M and H–O–H bending modes that often dominate the mid- and high-frequency spectra of hydrous oxides and hydroxides, many of the modes related to interlayer and surface species are essentially intermolecular. They often involve complex interactions among water molecules, interlayer or surface ions, and the substrate oxide or hydroxide layer. A combination of spectroscopic and computational approaches is the most effective way to address these issues.

Given that no spectroscopic information was used in the parametrization of CLAYFF, calculation of vibrational spectra can be a stringent test for validating the method used to develop the force field. Figure 10 illustrates the comparison between the experimentally obtained far-infrared spectrum for the LHD

phase of  $\text{LiAl}_2(\text{OH})_6\text{Cl}\cdot\text{H}_2\text{O}$  and an MD-derived power spectrum for the same material.<sup>89</sup> The power spectra were calculated as Fourier transformations of the velocity auto-correlation functions (VACF) obtained from the MD trajectories of the model system.<sup>90</sup>

In evaluating the agreement between computed power spectra and experimentally observed ones in Figure 10, it is important to keep in mind that the two are not physically identical, with the consequence that the calculated and experimental relative intensities of the spectral bands cannot be directly compared. The total computed power spectrum includes contributions from all atomic motions recorded in the VACF. In contrast, experimental infrared band intensities are related to fluctuations of the electric dipole moment due to atomic and molecular vibrations.<sup>21,91</sup> However, because each translating atom in the MD simulations bears a partial charge, all atomic motions contribute to the fluctuations of the electric dipole moment for the system. Therefore, the number of spectral bands and their positions in the observed and simulated spectra remain strongly related.

For  $\text{LiAl}_2(\text{OH})_6\text{Cl}\cdot\text{H}_2\text{O}$ , the five most prominent modes associated with vibrations of  $\text{LiAl}_2(\text{OH})_6$  octahedra and the interlayer species occur in the calculated power spectrum at about 90, 140, 190, 230, and 280  $\text{cm}^{-1}$ . They are in excellent agreement with the observed far-infrared band frequencies (Figure 10). Decomposition of the calculated power spectra into their *XX*, *YY*, and *ZZ* anisotropic components and contributions of individual atomic types shows that the higher frequency bands are associated with complex motions of Li and Al ions largely parallel to the hydroxide layers (*x*–*y* plane), while the lower frequency bands are due primarily to Al and Li motions in the direction perpendicular to the layers (*z*-direction), with a lesser contribution from hydroxyl O motions in the *x*–*y* plane. The translational vibrational motions of interlayer  $\text{Cl}^-$  ions and  $\text{H}_2\text{O}$  molecules contribute strongly to the lower frequency range of the spectrum, with the band near 90  $\text{cm}^{-1}$  due mainly to

molecular motions perpendicular to the layering (bending of  $\text{HOH}\cdots\text{Cl}\cdots\text{HO}$  bonds) and the band centered near  $200\text{ cm}^{-1}$  due to  $\text{H}_2\text{O}$  translational vibrations in the  $x$ - $y$  plane (stretching of  $\text{HOH}\cdots\text{Cl}$  bonds).

Similarly good results were recently obtained in the MD simulations for a series of LDH materials of various cationic and anionic compositions.<sup>81,89</sup> Accordingly, for a simple force field that does not explicitly include covalent bonds (except for  $\text{H}_2\text{O}$  and  $\text{OH}$ ), and that was not originally optimized to model clay minerals, LDH phases, or the vibrational properties of any materials, CLAYFF yields vibrational frequencies in the computed power spectra in surprisingly good agreement with the observed infrared spectra, demonstrating a great robustness of the developed force field. It is likely that agreement could be significantly improved in future force field models if the vibrational data are explicitly included in the force field parametrization.

## Conclusions

The development of a general set of interatomic potentials is of considerable importance for the molecular simulation of the structure, properties, and dynamics of hydrated and hydrous phases for numerous environmental and materials problems. The CLAYFF force field provides a general set of simple interatomic potentials that allow investigation into the complex behavior of natural hydrated materials, including hydroxides, oxyhydroxides, and clays. Traditional characterization and spectroscopic analysis investigations are extremely difficult due to the complex multicomponent chemistry, presence of water and hydroxyls, lack of quality single crystals for structural refinements, nanoscale particle sizes, large cation and water disorder states, stacking disorder for layered phases, among other limitations for these mineral phases. Molecular simulations provide an opportunity to test and validate candidate models for bulk structures, surfaces, interfaces, and aqueous solutions with experimental observations. Parametrization of CLAYFF using a set of simple structurally well-characterized hydrated phases allows good transferability of the force field parameters while maintaining full flexibility of all atoms and crystallographic cell parameters during energy minimization, molecular dynamics, and Monte Carlo simulations, thereby allowing for exchange of energy and momentum among all components of the system. An indirect justification of our approach to CLAYFF parametrization can be found in the recent thermochemical measurements of Allada et al.<sup>92</sup> who demonstrated that the thermodynamic properties of mixed layered hydroxides can be quite accurately estimated by treating them as a mixture of structurally similar binary compounds. This mechanical-mixture approach works on the atomistic scale because the metal and anion coordination environments are structurally similar, and therefore also energetically similar, to those in the simple phases used as components. These are, basically, the same model phases we used for CLAYFF parametrization.

Specific highlights of CLAYFF include the ability to distinguish between tetrahedral and octahedral aluminum, and to accurately delocalize partial charges among coordinating oxygens when substituting atoms on various tetrahedral and octahedral sites. CLAYFF accurately describes the bulk structures of a broad range of simple hydroxide and oxyhydroxide phases. More complex systems such as the structures, surfaces, and interfaces associated with clays and layered double hydroxides as well as cement-related phases are also successfully simulated. Furthermore, the use of a simple nonbonded interaction potential to describe metal-oxygen bonds and harmonic

terms to describe water and hydroxyl bonding provides an efficient and accurate basis for simulating large systems involving thousands to millions of atoms.

**Acknowledgment.** We acknowledge the constructive reviews and comments provided by two anonymous referees. Louise Criscenti, James Kirkpatrick, and Henry Westrich also provided suggestions that contributed to an improved manuscript. Many thanks are due to Jianwei Wang for providing access to his structure and hydration data on hydrotalcite. Computations utilized the Cerius<sup>2</sup> Version 4.0 software package from Accelrys Inc. The senior author is appreciative of funding provided by the U.S. Department of Energy, Office of Basic Energy Sciences, Geosciences Research and the U.S. Nuclear Regulatory Commission, Office of Nuclear Regulatory Research. Sandia is a multiprogram laboratory operated by Sandia Corp., a Lockheed Martin company, for the U.S. Department of Energy under contract DE-AC04-94AL85000.

## References and Notes

- (1) Young, R. A.; Hewat, A. W. *Clays Clay Miner.* **1996**, *36*, 225.
- (2) Bish, D. L. *Clays Clay Miner.* **1993**, *41*, 783.
- (3) Delville, A. *Langmuir* **1991**, *7*, 547.
- (4) Delville, A. *Langmuir* **1992**, *8*, 1796.
- (5) Delville, A. *J. Phys. Chem.* **1995**, *99*, 2033.
- (6) Skipper, N. T.; Chang, F. C.; Sposito, G. *Clays Clay Miner.* **1995**, *43*, 285.
- (7) Skipper, N. T.; Refson, K.; McConnell, J. D. C. *Clay Minerals* **1989**, *24*, 411.
- (8) Skipper, N. T.; Refson, K.; McConnell, J. D. C. *J. Chem. Phys.* **1991**, *94*, 7434.
- (9) Skipper, N. T.; Sposito, G.; Chang, F. C. *Clays Clay Miner.* **1995**, *43*, 294.
- (10) Sposito, G.; Park, S. H.; Sutton, R. *Clays Clay Miner.* **1999**, *47*, 192.
- (11) Chang, F. C.; Skipper, N. T.; Sposito, G. *Langmuir* **1995**, *11*, 2734.
- (12) Chang, F. C.; Skipper, N. T.; Sposito, G. *Langmuir* **1997**, *13*, 2074.
- (13) Greathouse, J. A.; Refson, K.; Sposito, G. *J. Am. Chem. Soc.* **2000**, *122*, 11459.
- (14) Greathouse, J.; Sposito, G. *J. Phys. Chem. B* **1998**, *102*, 2406.
- (15) Smith, D. E. *Langmuir* **1998**, *14*, 5959.
- (16) Hartzell, C. J.; Cygan, R. T.; Nagy, K. L. *J. Phys. Chem. A* **1998**, *102*, 6722.
- (17) Cygan, R. T. Molecular modeling in mineralogy and geochemistry. In *Reviews in Mineralogy and Geochemistry: Molecular Modeling Theory: Applications in the Geosciences*; Cygan, R. T., Kubicki, J. D., Eds.; The Geochemical Society: Washington, DC, 2001; pp 1.
- (18) Hobbs, J. D.; Cygan, R. T.; Nagy, K. L.; Schultz, P. A.; Sears, M. P. *Am. Mineral.* **1997**, *82*, 657.
- (19) Smrcok, L.; Benco, L. *Am. Mineral.* **1996**, *81*, 1405.
- (20) Bridgeman, C. H.; Buckingham, A. D.; Skipper, N. T. *Mol. Phys.* **1996**, *89*, 879.
- (21) Bougeard, D.; Smirnov, K. S.; Geidel, E. *J. Phys. Chem. B* **2000**, *104*, 9210.
- (22) Teppen, B. J.; Rasmussen, K.; Bertsch, P. M.; Miller, D. M.; Schäfer, L. *J. Phys. Chem.* **1997**, *B101*, 1579.
- (23) Hill, J. R.; Sauer, J. *J. Phys. Chem.* **1995**, *99*, 9536.
- (24) Dauber-Osguthorpe, P.; Roberts, V. A.; Osguthorpe, D. J.; Wolff, J.; Genest, M.; Hagler, A. T. *Proteins: Struct. Funct. Genet.* **1988**, *4*, 31.
- (25) Ermoshin, V. A.; Smirnov, K. S.; Bougeard, D. *Chem. Phys.* **1996**, *209*, 41.
- (26) Ermoshin, V. A.; Smirnov, K. S.; Bougeard, D. *Surf. Sci.* **1996**, *368*, 147.
- (27) Smirnov, K. S.; Bougeard, D. *J. Phys. Chem. B* **1999**, *103*, 5266.
- (28) Ermoshin, V. A.; Smirnov, K. S.; Bougeard, D. *Chem. Phys.* **1996**, *202*, 53.
- (29) Sainz-Diaz, C. I.; Hernández-Laguna, A.; Dove, M. T. *Phys. Chem. Miner.* **2001**, *28*, 130.
- (30) Berendsen, H. J. C.; Postma, J. P. M.; van Gunsteren, W. F.; Hermans, J. Interaction models for water in relation to protein hydration. In *Intermolecular Forces*; Pullman, B., Ed.; D. Reidel: Amsterdam, 1981; pp 331.
- (31) Berendsen, H. J. C.; Grigera, J. R.; Straatsma, T. P. *J. Phys. Chem.* **1987**, *91*, 6269.
- (32) Smith, D. E.; Dang, L. X. *J. Chem. Phys.* **1994**, *100*, 3757.
- (33) van der Spoel, D.; van Maaren, P. J.; Berendsen, H. J. C. *J. Chem. Phys.* **1998**, *108*, 10220.



- (34) Kalinichev, A. G.; Kirkpatrick, R. J.; Cygan, R. T. *Am. Mineral.* **2000**, *85*, 1046.
- (35) Kalinichev, A. G.; Wang, J.; Kirkpatrick, R. J.; Cygan, R. T. Molecular dynamics simulation of layered double hydroxides. In *Foundations of Molecular Modeling and Simulation, Proceedings of the First International Conference on Molecular Modeling and Simulation*; Cummings, P. T., Westmoreland, P. R., Eds.; American Institute of Chemical Engineers, 2001; Vol. 97, pp 251.
- (36) Hou, X. Q.; Kalinichev, A. G.; Kirkpatrick, R. J. *Chem. Mater.* **2002**, *14*, 2078.
- (37) Teleman, O.; Jonsson, B.; Engstrom, S. *Mol. Phys.* **1987**, *60*, 193.
- (38) Gale, J. D. *J. Chem. Soc., Faraday Trans.* **1997**, *93*, 629.
- (39) Gale, J. D. *Philos. Mag. B* **1996**, *73*, 3.
- (40) Lepage, Y.; Calvert, L. D.; Gabe, E. J. *J. Phys. Chem. Solids* **1980**, *41*, 721.
- (41) Maslen, E. N.; Streltsov, V. A.; Streltsova, N. R.; Ishizawa, N.; Satow, Y. *Acta Crystallogr. Sect. B, Struct. Sci.* **1993**, *49* (Part 6), 973.
- (42) Christensen, A. N.; Lehmann, M. S.; Convert, P. *Acta Chem. Scand.* **1982**, *36*, 303.
- (43) Hill, R. J. *Phys. Chem. Miner.* **1979**, *5*, 179.
- (44) Saalfeld, H.; Wedde, M. Z. *Kristallogr.* **1974**, *139*, 129.
- (45) Mulliken, R. S. *J. Chem. Phys.* **1955**, *23*, 1833.
- (46) Chirlian, L. E.; Francl, M. M. *J. Comput. Chem.* **1987**, *8*, 894.
- (47) Breneman, C. M.; Wiberg, K. B. *J. Comput. Chem.* **1990**, *11*, 361.
- (48) Delley, B. *J. Chem. Phys.* **1990**, *92*, 508.
- (49) Delley, B. *J. Chem. Phys.* **2000**, *113*, 7756.
- (50) Perdew, J. P.; Wang, Y. *Phys. Rev. B: Condens. Matter* **1992**, *45*, 13244.
- (51) Tosi, M. P. *Solid State Phys.* **1964**, *131*, 533.
- (52) Szytula, A.; Burewicz, A.; Dimitrijevic, K., S.; Rzany, H.; Todorovic, J.; Wanic, A.; Wolksi, W. *Phys. Status Solidi* **1986**, *26*, 429.
- (53) Kondrashev, Y. D.; Omel'chenko, Y. A. *Zh. Neorg. Khim.* **1964**, *9*, 512.
- (54) Catti, M.; Ferraris, G.; Hull, S.; Pavese, A. *Phys. Chem. Miner.* **1995**, *22*, 200.
- (55) Desgranges, L.; Grebille, D.; Calvarin, G.; Chevrier, G.; Floquet, N.; Niepce, J. C. *Acta Crystallogr. Sect. B, Struct. Sci.* **1993**, *49* (Part 5), 812.
- (56) Zintl, E.; Harder, A.; Dauth, B. Z. *Elektrochem.* **1934**, *40*, 588.
- (57) Halgren, T. A. *J. Am. Chem. Soc.* **1992**, *114*, 7827.
- (58) Rappé, A. K.; Casewit, C. J.; Colwell, K. S.; Goddard, W. A.; Skiff, W. M. *J. Am. Chem. Soc.* **1992**, *114*, 10024.
- (59) Smith, D. E.; Dang, L. X. *J. Chem. Phys.* **1994**, *101*, 7873.
- (60) Koneshan, S.; Rasaiah, J. C.; LyndenBell, R. M.; Lee, S. H. *J. Phys. Chem. B* **1998**, *102*, 4193.
- (61) Åqvist, J. *J. Phys. Chem.* **1990**, *94*, 8021.
- (62) Brigatti, M. F.; Lugli, C.; Montorsi, S.; Poppi, L. *Clays Clay Miner.* **1999**, *47*, 664.
- (63) Laird, D. A. *Clays Clay Miner.* **1999**, *47*, 630.
- (64) Lee, J. H.; Guggenheim, S. *Am. Mineral.* **1981**, *66*, 350.
- (65) Farmer, V. C. *The Infrared Spectra of Minerals*; Mineralogical Society: London, 1974.
- (66) Karasawa, N.; Goddard, W. A. *J. Phys. Chem.* **1989**, *93*, 7320.
- (67) Leach, A. R. *Molecular Modeling Principles and Applications*; Addison Wesley Longman Limited: Essex, U.K., 1996.
- (68) Parrinello, M.; Rahman, A. *J. Appl. Phys.* **1981**, *52*, 7182.
- (69) Verlet, L. *Phys. Rev.* **1967**, *159*, 98.
- (70) Brindley, G. W. Order-disorder in clay mineral structures. In *Crystal Structures of Clay Minerals and their X-Ray Identification*; Brindley, G. W., Brown, G., Eds.; Mineralogical Society: London, 1980; pp 125.
- (71) Tsipursky, S. I.; Drits, V. A. *Clay Minerals* **1984**, *19*, 177.
- (72) Fu, M. H.; Zhang, Z. Z.; Low, P. F. *Clays Clay Miner.* **1990**, *38*, 485.
- (73) Karaborn, S.; Smit, B.; Heidug, W.; Urai, J.; Oort, v. *Science* **1996**, *271*, 1102.
- (74) Hensen, E. J. M.; Smit, B. *J. Phys. Chem. B* **2002**, *106*, 12664.
- (75) Kaneyoshi, M.; Jones, W. J. *Mater. Chem.* **1999**, *9*, 805.
- (76) Chisem, I. C.; Jones, W. J. *Mater. Chem.* **1994**, *4*, 1737.
- (77) Newman, S. P.; Jones, W. J. *Solid State Chem.* **1999**, *148*, 26.
- (78) Hou, X. Q.; Kirkpatrick, R. J.; Yu, P.; Moore, D.; Kim, Y. *Am. Mineral.* **2000**, *85*, 173.
- (79) Wang, J.; Kalinichev, A. G.; Kirkpatrick, R. J.; Hou, X. *Chem. Mater.* **2001**, *13*, 145.
- (80) Kalinichev, A. G.; Kirkpatrick, R. J. *Chem. Mater.* **2002**, *14*, 3539.
- (81) Wang, J.; Kalinichev, A. G.; Amonette, J. E.; Kirkpatrick, R. J. *Am. Mineral.* **2003**, *88*, 398.
- (82) Fogg, A. M.; Rohl, A. L.; Parkinson, G. M.; O. Hare, D. *Chem. Mater.* **1999**, *11*, 1194.
- (83) Newman, S. P.; Williams, S. J.; Coveney, P. V.; Jones, W. J. *Phys. Chem. B* **1998**, *102*, 6710.
- (84) Aicken, A. M.; Bell, I. S.; Coveney, P. V.; Jones, W. *Adv. Mater.* **1997**, *9*, 496.
- (85) Bellotto, M.; Rebours, B.; Clause, O.; Lynch, J.; Bazin, D.; Elkaim, E. *J. Phys. Chem.* **1996**, *100*, 8527.
- (86) Titulaer, M. K.; Talsma, H.; Jansen, J. B. H.; Geus, J. W. *Clay Minerals* **1996**, *31*, 263.
- (87) Bocclair, J. W.; Braterman, P. S.; Brister, B. D.; Yarberr, F. *Chem. Mater.* **1999**, *11*, 2199.
- (88) Klopogge, J. T. *The Application of Vibrational Spectroscopy to Clay Minerals and Layered Double Hydroxides*; The Clay Minerals Society: Boulder, 2004.
- (89) Kirkpatrick, R. J.; Kalinichev, A. G.; Wang, J.; Hou, X. Q.; Amonette, J. E. Molecular modeling of the vibrational spectra of surface and interlayer species of layered double hydroxides and other layer-structure materials. In *The Application of Vibrational Spectroscopy to Clay Minerals and Layered Double Hydroxides*; Klopogge, J. T., Ed.; The Clay Minerals Society: Boulder, 2004 (in press).
- (90) McQuarrie, D. A. *Statistical Mechanics*; Harper and Row: New York, 1976.
- (91) Kagunya, W.; Baddour-Hadjean, R.; Kooli, F.; Jones, W. *Chem. Phys.* **1998**, *236*, 225.
- (92) Allada, R. K.; Navrotsky, A.; Berbeco, H. T.; Casey, W. H. *Science* **2002**, *296*, 721.